



Trans. Nonferrous Met. Soc. China 30(2020) 2697-2708

Transactions of Nonferrous Metals Society of China

www.tnmsc.cn



Cracking mechanism in as-cast GH4151 superalloy ingot with high γ' phase content

Xin-xu LI^{1,2}, Chong-lin JIA², Yong ZHANG², Shao-min LÜ², Zhou-hua JIANG¹

- 1. School of Metallurgy, Northeastern University, Shenyang 110819, China;
- 2. Beijing Institute of Aeronautical Materials, Aero Engine Corporation of China, Beijing 100095, China

Received 26 January 2020; accepted 16 July 2020

Abstract: The fundamental mechanism of the cracking formation was investigated for the as-cast GH4151 superalloy. By analyzing the characteristics of cracking, the cracking mechanism was determined to be the cold crack formed during the cooling process. And cold cracking is closely related to severe segregation, complex precipitates and uneven γ' phase distribution. During cooling process, cracks were generated around the precipitates due to their different linear shrinkage coefficients. The annealing treatment process controlling the residual stress, the size and morphology of γ' phase was proposed. The annealing treatment plays a role in reducing residual stress through decreasing the thermal gradient and controlling the size distribution of γ' phase to reduce the strain concentration around the precipitate phases.

Key words: GH4151 alloy; as-cast ingot; cracking mechanism; residual stress; γ' phase

1 Introduction

Nickel-based superalloys are important structural materials for the turbine [1,2]. The increased thrust-to-weight ratio in advanced aircraft requires higher inlet temperature and higher efficiency for the turbine [3], which demands excellent high temperature mechanical properties. In order to meet the critical demands for high applications, temperature some strengthened elements such as Nb, Ti and Mo are added into the superalloy [4]. GH4151 alloy is a newly nickelbased wrought superalloy, whose optimized compositions have been designed with 3.4% Nb and total content of Al, Ti, and Nb up to around 10%. Severe segregation and complex precipitate phases would promote the formation of cracks. Once the crack appears in the ingot, subsequent processing cannot be carried out further. Therefore, it is of great practical significance to reveal the mechanism of crack formation and propose control measures for GH4151 alloy.

Over the several decades, much effort has been made to understand fundamental mechanisms about hot tearing [5]. Some scholars [6,7] considered that hot tears develop in the last stage of the solidification when the volume fraction of solid phase is high and liquid feeding is hindered. Subsequently, the remaining liquid film has no sufficient resistance against stresses due to the volume contraction being related to the liquid-tosolid phase transformation and the thermal contraction in the solid. In some cases, the two solid sides are able to coalesce with dendritic growth and the solid bridge is formed when the volume fraction of solid phase is higher. However, the solid bridge will deform upon further pulling during the opening of the hot tear [8]. ESKIN et al [9] revealed the mechanisms associated with crack and predicted the

DOI: 10.1016/S1003-6326(20)65413-9

crack criterion. In the views of some researchers, solidification cracking was attributed to the formation of low melting point liquid films or phases [10–12]. WANG et al [13] and CHAUVET et al [14] suggested that high angle GBs are prone to solidification cracking development because high angle GBs have higher grain boundary energy values.

Several theoretical mechanisms have been proposed to explain cold cracking. DREZET et al [15] holds the views that cold cracking usually occurs when ingots are cooled below 200 °C and is mainly caused by the release of elastic residual strain energy stored in the ingots. There is a general opinion that cold cracking is intergranular fracture, but transgranular fracture features can also be noticed because of the catastrophic propagation of cold cracking [16].

At present, very limited information regarding the cold cracking for superalloy has been reported. In this study, optical microscope (OM), scanning electron microscopy (SEM), X-ray diffraction (XRD) detection and electron probe micro-analyzer (EPMA) were employed to investigate the fundamental mechanism governing the formation process of cracking on as-cast GH4151 superalloy.

2 Experimental

2.1 Materials

The material used in the present work was prepared by using vacuum induction melting (VIM) and electroslag remelting (ESR). The diameter of VIM ingot was 280 mm. The main chemistry composition of VIM ingot was 3.7% Al, 2.8% Ti, 3.4% Nb, 11.9% Cr, 4.5% Mo, 15.3% Co, 2.7% W, 0.5% V, 0.06% C, and balance Ni (in mass fraction). And then VIM ingot was cut into two parts as ESR electrodes, whose corresponding ESR ingots were named E1 and E2. After remelting, ESR ingot E1 was cooled by sand cooling and E2 was put into a heat treatment furnace within 1000 °C and was kept at the temperature for 4 h before furnace cooling. The diameter of ESR ingot was 350 mm. The main composition of ESR ingot E1 was 3.6% Al, 2.7% Ti, 3.4% Nb, 11.8% Cr, 4.4% Mo, 15.1% Co, 2.6% W, 0.5% V, 0.06% C, and balance Ni, and main composition of E2 was 3.7% Al, 2.7% Ti, 3.4% Nb, 11.7% Cr, 4.5% Mo, 2.6% W, 15.2% Co, 0.5% V, 0.06% C, and balance Ni (mass fraction).

2.2 Experimental process and test scheme of residual stress

The measuring equipment selected in this experiment is PROTO LXRD residual stress testing equipment, and the measured stress is surface stress with a depth of 60-80 µm. The samples used for residual stress testing were cut from the cross-section of the ingot. The surface of sample was machined by technology of high feed milling. In order to reduce the stress caused by sample preparation, the sample was left for two months in the air after milling. In addition, surface of the sample was degreased before the measurements. X-ray tube with Mn anode was used for residual stress detection of the material. The test voltage was 30 kV and the current was 25 mA. In this experiment, 15 test points were selected from the diameter length of the ingot cross-section on average to measure the residual stress. The Hdirection was along the diameter, and the Xdirection was perpendicular to the diameter.

2.3 XRD phase identification

The sample of 8 mm \times 20 mm \times 40 mm was cut from ingot E1 and electrolyzed on the DC power device. The electrolyte was $C_3H_8O_3$ (50 mL) + HCl (50 mL) + $C_6H_8O_7$ (10 g) + CH₃OH (900 mL), the current density was 0.1–0.2 A/cm², and the electrolytic temperature was 0–5 °C. The powder obtained was tested on a D8 Discover XRD equipment, and the results were calibrated on Jade 6.5. The lattice parameters of the phases corresponding to the peaks are available from the PDF database on Jade 6.5.

2.4 JmatPro simulation

Some thermodynamic properties can be calculated by Java based material properties (JmatPro) for most Ni-based superalloys. Hence, JmatPro and a Ni-based superalloy database were used to calculate the volume change of different temperature. Different phases with compositions were input into the program to calculate volume change in the "phases and solidification" properties of module. temperature range of the simulation was set from 20 to 1500 °C. The simulation returned results at intervals of 5 °C until the fraction of liquid was 0.02. The purpose of simulation in this work was only to show the volume change of these components corresponding to different phases in the solidification process, and the phase transition at different temperatures was ignored.

2.5 Microstructure examination

The observation of macrostructure of ingot was conducted by soaking for 20 min using FeCl₃ hydrochloric acid solution. The specimens for OM and SEM observation were prepared in the solutions of Cr₂O₃ (15 g) + H₃PO₄ (150 mL) + H₂SO₄ (10 mL) and etched electrolytically at 3–4 V in an aqueous solution of 10% phosphoric acid, respectively. Leica DM6000M optical microscope and Quanta 200FEG scanning electron microscope were employed to observe microstructure. An electron probe microanalyzer (EPMA: JXA–8100) was employed to quantitatively measure chemical compositions and types of precipitates.

3 Results and discussion

3.1 Cracking characterization

Figure 1 shows the macroscopic morphology of ESR ingot E1 with a diameter of 350 mm and a thickness of 15 mm. It can be seen from Fig. 1(a) that a crack appears almost across the ESR ingot E1. The width of crack in the center of ESR ingot E1 is the largest on the cross-section of the ingot, reaching around 2 mm. This characteristic indicates that the crack originates from the center of ESR ingot E1 and then extends to the edge of the ingot. This phenomenon could be easy to understand. The central part of the ingot was solidified at the last stage of the whole solidification process, thus central part possessed the highest temperature, whose strength and plasticity were very low. The edge of the ingot was solidified completely due to the high cooling rates, so secondary dendrite spacing, segregation and the size and number of brittle phases are smaller, resulting in higher strength and plasticity of the edge than those of the center. In this case, when volume changes occurred due to solidification shrinkage of the ingot, the central portion of the ingot would begin to crack due to the low strength. As soon as a crack formed in the center of the ingot, stress concentration occurred at the crack tip, and then crack expanded along the direction of stress concentration. Therefore, the macroscopic crack morphology was formed, as shown in Fig. 1(a).



Fig. 1 Macroscopic morphologies of ESR ingot E1: (a) Macroscopic morphology of cracking; (b) Fracture morphology and longitudinal macrostructure

The fracture morphology and longitudinal macrostructure of the ingot are shown in Fig. 1(b). The dendrite skeleton morphology can be clearly seen on the fracture surface. The cracking morphology on the fracture surface is consistent with macro-structural dendrite morphology, indicating that the crack was formed and extended along the interdendritic region.

The fracture microstructure under SEM observation is shown in Fig. 2. It is illustrated in Fig. 2(a) that the surface of fracture exhibited dendritic morphology and was oxidized, indicating that the crack has been generated at high temperature and extended along the interdendrites. A typical brittle rupture rather than trace of molten liquid was retained in smaller regions of fracture surface, as seen in Fig. 2(b). These observations indicated hot tearing mechanisms. Therefore, it is characteristic of cold cracking. In other words, cracking most likely occurred at cooling stage after solidification. Moreover, some researchers also found that cold cracks present along the centreline of ingot [17], as shown in Fig. 1(a).

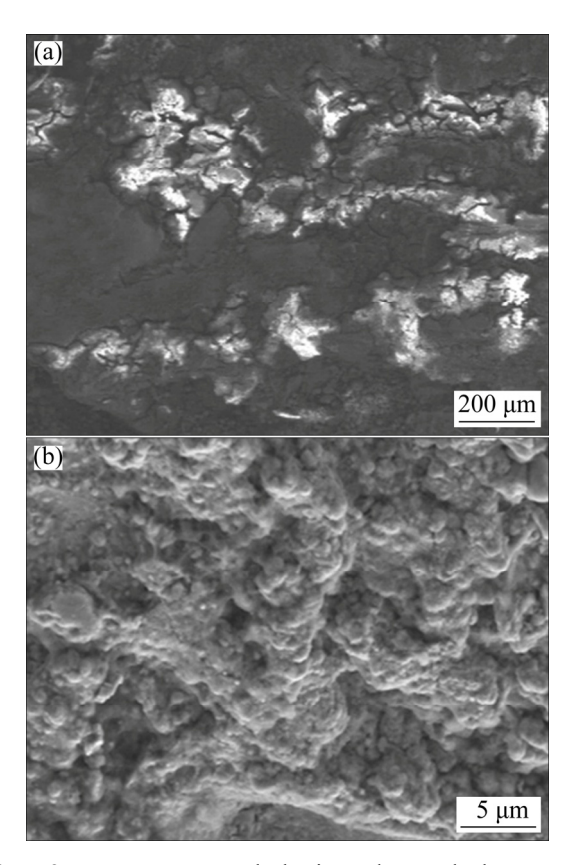


Fig. 2 Fracture morphologies detected by SEM: (a) Oxidized surface fracture; (b) Fracture surface in smaller regions

Figure 3(a) shows the dendrite morphology near the crack interfaces. It can be seen that the grain orientations on sides of the crack are different, that is, the crack is formed along the grain boundary. As soon as the crack is generated, it would propagate along the interdendrites except along the grain boundary, as shown in Fig. 3(b). Therefore, it can be inferred that the grain boundary and interdendrites are two relatively weak positions, which would become the path of crack propagation once they are subjected to greater external stress. Below solidus, brittle precipitates on the interdendritic/intergranular spaces make the material prone to intergranular brittle fracture [18,19].

Viewing the etched sample in the FESEM images (Fig. 4) using backscattered electron imaging confirmed that the cracking ended in the precipitate phases of the interdendrite and the crack propagated along the grain boundary, where there exist some fine white phases. Cold cracking is closely related to the ductility of the as-cast GH4151 alloy and stress can be released after sufficient plastic deformation. It is worth

mentioning that cracks mainly propagate along the grain boundaries and interdendritic region where the brittle intermetallics are located [20]. Therefore, in order to further comprehend cracking mechanism, it is necessary to explore basic properties of GH4151 alloy, such as identification of precipitates and segregation behavior.

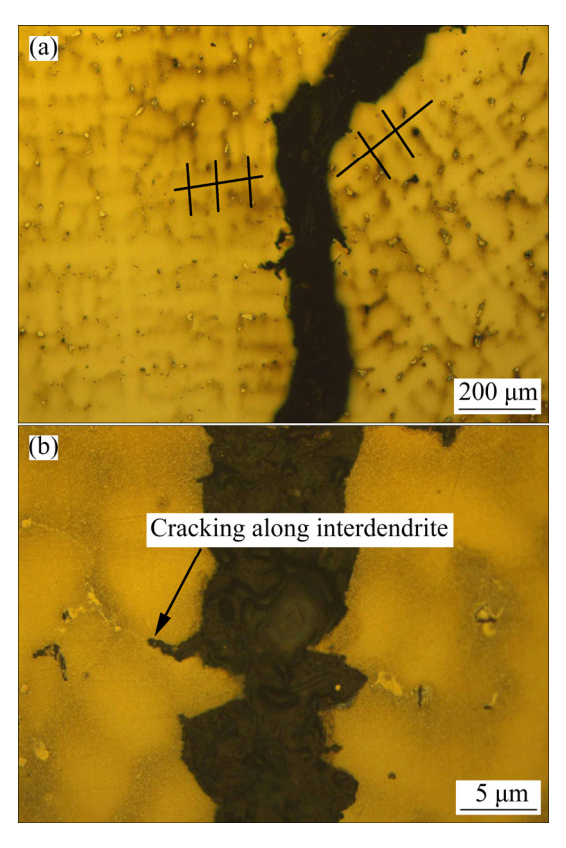


Fig. 3 Microstructures of crack: (a) Crack occurring along grain boundary; (b) Crack propagating along grain boundary

In order to characterize the minor secondary phases, the method of electrolytic extraction was implemented. Most of the matrix phases and γ' phases were removed by electrolytic corrosion, and the obtained powders contained minor secondary phases of GH4151 alloy. Based on the XRD results in Fig. 5, γ matrix, γ' phase, (Nb,Ti)C carbides, η phase, Laves phase and Ni₅Ce phase were found in as-cast GH4151 alloy. γ' phase is a face-centered cube, and its lattice constant a is 0.3581 nm. (Nb,Ti)C carbide is a face-centered cube, and its lattice constant a is 0.4427 nm. η phase is a hexagonal close-packed structure, and its lattice constants a and b are both 0.5092 nm and c is 0.8297 nm. Laves phase is also a hexagonal closepacked structure, and its lattice constants a and b

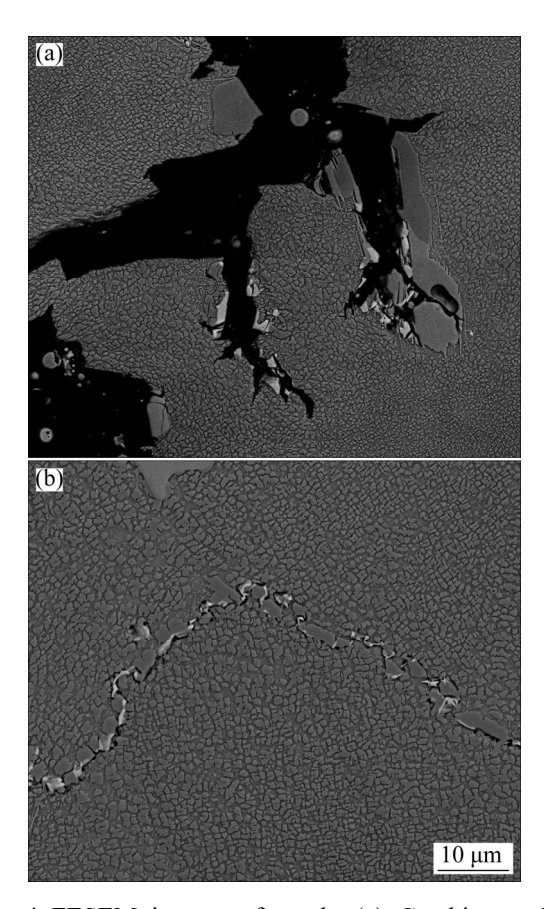


Fig. 4 FESEM images of crack: (a) Cracking ending in precipitate phases of interdendrite; (b) Crack propagating along grain boundary

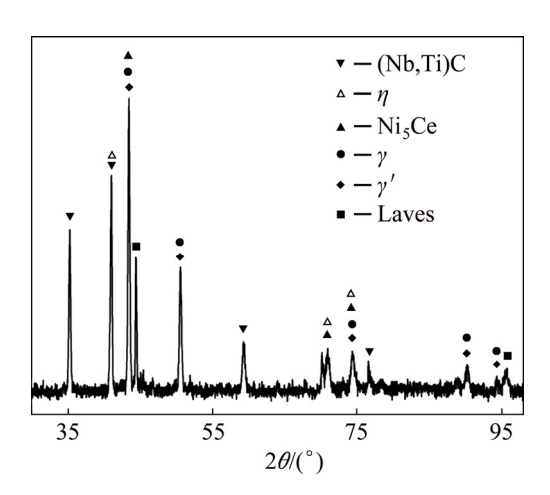


Fig. 5 XRD pattern of as-cast GH4151 alloy

are both 0.4730 nm and c is 0.7720 nm. Ni₅Ce phase is a hexagonal crystal structure, and its lattice constants a and b are both 0.4875 nm and c is 0.4010 nm.

The microstructure of the alloy in interdendritic regions is complex, as shown in Fig. 6. Figures 6(a) and (b) show the morphologies of the secondary phases under SEM and EPMA,

respectively. The secondary phases in the interdendritic areas can be identified based on their chemistry composition determined by EDS in Table 1. However, the Ni₅Ce phase cannot be detected under SEM observation. The EPMA image of Ni₅Ce is shown in Fig. 6(b), and the composition of precipitation particle determined by EPMA is listed in Table 1. The Ni₅Ce phase is always located around Laves phase, indicating that it is precipitated after the formation of Laves phase. Therefore, combining with the results above, it can be concluded that secondary phases of GH4151 alloy consist of carbide, η phase, eutectic $\gamma + \gamma'$, Laves Ni₅Ce phase. The results of phase and microstructure observation are in consistency with the results of XRD analysis. In addition, there exist γ' phases with different sizes in the dendrite and interdendrite regions, as shown in Fig. 6(a). This is mainly due to segregation behavior during the solidification. The quantitative analysis of the segregation was performed by EPMA, and the results are shown in Table 2. A segregation coefficient k was defined for elements as the ratio of the average content in the interdendrite area to

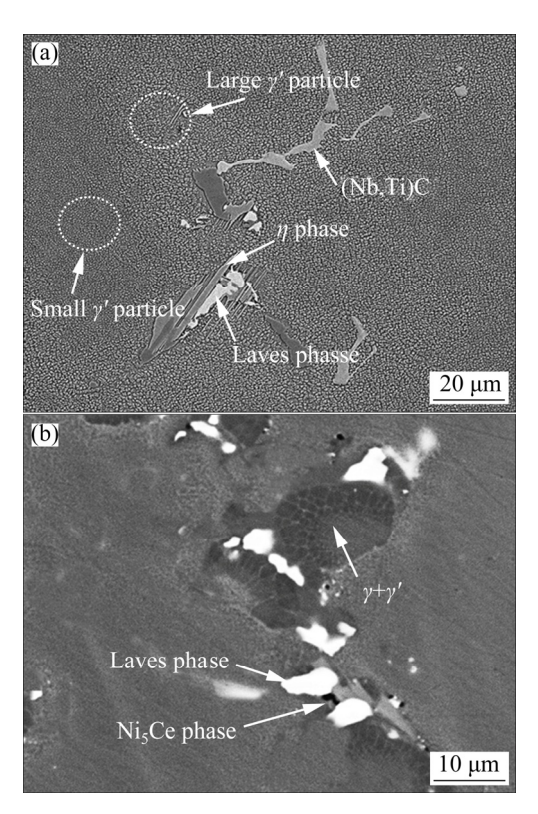


Fig. 6 Microstructures of GH4151 alloy ingot in interdendritic regions: (a) Morphology of secondary phase under SEM; (b) Morphology of secondary phase under EPMA

Table 1 EDS and EPMA analysis of secondary phase (wt.%)

Phase	Ni	Co	Cr	W	Al	Mo	V	Nb	Ti	С	Се
γ+γ'	60.377	13.054	3.972	0.882	4.411	2.788	0.235	5.489	5.535	0.151	_
(Nb,Ti)C	3.4	0.9	1.0	3.6	_	4.9	0.8	54.5	18.9	11.1	_
η	57.9	15.4	4.2	1.9	2.7	1.2	0.1	9.8	6.8	_	_
Laves	22.856	18.852	16.069	3.502	0.444	18.572	0.223	17.564	0.969	0.382	_
Ni ₅ Ce	66.95	9.35	3.67	0	0.87	0	0	2.28	0	0	16.10

Table 2 Quantitative analysis of segregation of GH4151 alloy

Phase	Phase Parameter		Ti	Ni	W	Nb	Cr	Mo	Co
Dendrite	Mean content/wt.%	3.44	2.85	56.7	2.79	2.08	12.06	3.73	15.53
	Standard deviation/%	0.21	0.32	1.2	0.18	0.19	1.11	0.27	1.25
Interdendrite	Mean content /wt.%	3.1	4.39	55.24	1.65	5.61	10.13	4.65	14.51
	Standard deviation/%	0.19	0.29	1.3	0.21	0.18	1.02	0.28	1.14
	0.9	1.54	0.97	0.59	2.7	0.84	1.25	0.93	

that in the dendrite area. The segregation inclination of Nb, Ti and some elements is relatively large, which results in the formation of complex precipitate phases in the interdendrites, as well as different size distributions of γ' phase.

According to EDS analysis on composition of phases, Jmatpro software was used to calculate the volume change of different phases with temperature, as shown in Fig. 7. As illustrated in Fig. 7, the volume changes of different phases with temperature are quite different, especially for (Nb,Ti)C phase. Therefore, strain was generated around the precipitate phases and finally cracks appeared due to their different linear shrinkage coefficients. This phenomenon occurred in the preparation process of the ingot, as shown in Fig. 8.

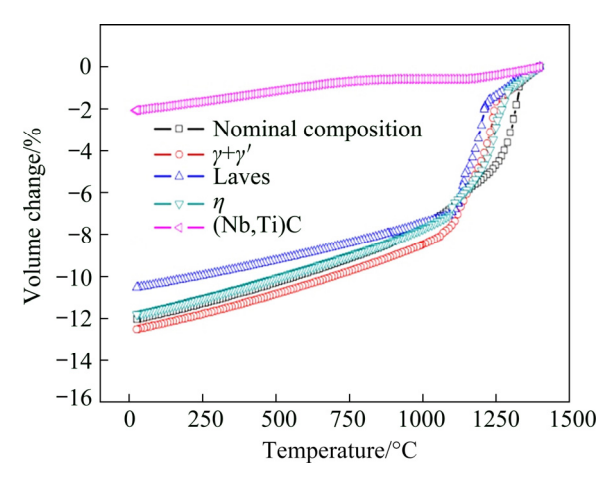


Fig. 7 Volume change of different phases at different temperatures

Cracks appeared at the boundaries of these phases or in these phases. Thus, (Nb, Ti)C, Laves phase, η phase and $\gamma+\gamma'$ eutectic would be the source of cracking during preparation process of the ingot. It is also seen that the proportions of these precipitate phases are in accordance with Nb contents. That is to say, with the increase of Nb content, cold cracking tendency is also increased.

3.2 Reasons for crack formation

During cooling process, the stored elastic strain energy, which is developed due to heat shrinkage, would reach a certain critical value and then cold cracking of GH4151 ingot is formed. The residual stress values on 15 test points along the cross-sectional diameter of GH4151 ingot are shown in Table 3. At each test point, residual stresses were tested in two directions, where H direction is along the diameter and X direction is perpendicular to the diameter. The direct factor of crack formation is the local strain generated by solidification shrinkage. When the internal stress exceeds the bearing capacity of the alloy, that is, the residual stress is greater than the tensile strength of the alloy, the cracking will occur in the ingot. The cracking will occur when either the maximum principal stress reaches the uniaxial tensile strength or the minimum principal stress reaches the uniaxial compressive strength [21]. Due to segregation of the ingot, the residual stresses are very different in dendritic, interdendritic and brittle phase regions,

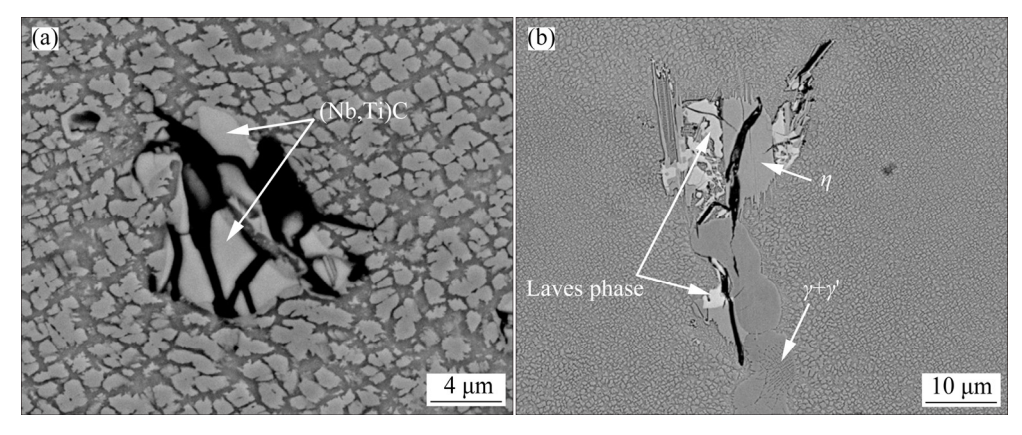


Fig. 8 Cracks appearing around precipitate phases

Table 3 Residual stress on 15 test points of GH4151 alloy (MPa)

anoy (vii a)								
Test	<i>H</i> di	rection	<i>X</i> di	X direction				
point	Mean	Standard	Mean	Standard				
	Mean	deviation	Mean	deviation				
1	171.11	10.34	1256.01	102.12				
2	392.92	11.21	892.55	43.23				
3	-165.46	27.12	664.49	63.72				
4	1191.6	23.21	1056.67	21.82				
5	572.85	14.12	795.37	12.34				
6	798.16	21.87	509.01	57.39				
7	443.98	19.98	850.15	56.82				
8	186.4	11.11	1352.42	123.72				
9	443.68	25.82	1295.63	109.72				
10	1193.98	32.19	-343.89	41.21				
11	377.48	21.75	-644.58	23.76				
12	352.1	23.85	206.6	19.81				
13	-307.96	17.69	-350.84	34.28				
14	1708.94	132.65	1573.72	138,74				
15	43.69	12.13	220.74	38.76				

Negative values represent compressive stress and other values represent tensile stress

and thus the values are scattering. Tensile property of the ingot was tested and its room tensile strength is 807 MPa. As shown in Table 3, a high residual stress is developed, exceeding 1700 MPa in some locations, which is bound to exceed the tensile strength of the ingot. When the residual stress exceeds the tensile strength of the ingot, deformation and even fracture may occur.

Residual stress is composed of thermal stress caused by temperature gradient and structure stress caused by precipitation and segregation. Severe segregation, complex precipitate phases and high content of γ' phase make the microstructure

stress of GH4151 alloy greater, as shown in Fig. 6. The cold cracking tendency is consistent with the nonequilibrium precipitate contents of GH4151 under a given solidification process. It has a huge possibility that massive nonequilibrium precipitates located in interdendritic region and grain boundaries greatly decrease the ductility of as-cast GH4151 alloys. In addition, high γ' phase contents and the size and morphology of γ' phase also influence the ductility of as-cast GH4151 alloys.

In view of the cause for cracking formation of GH4151 alloy, an annealing process controlling the residual stress, the size and morphology of γ' phase was proposed.

3.3 Effects of annealing treatment on microstructure and properties

Figure 9 shows the macrostructure of the ESR ingot E2 after annealing process. Obviously, no cracks appeared in the ingot, indicating that the

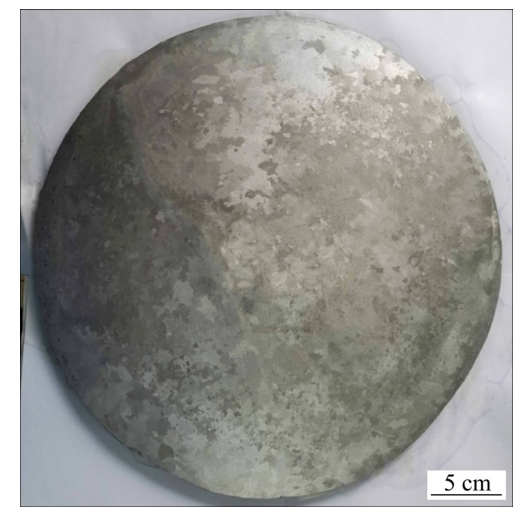


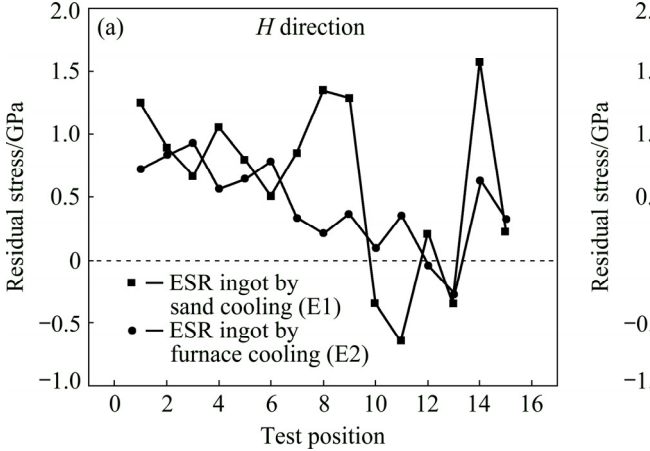
Fig. 9 Macroscopic morphology of ESR ingot E2 after annealing process

formation of cracks was effectively suppressed through the annealing process.

The residual stress of ESR ingot E2 was measured on the cross-section. The comparison of residual stresses for ESR ingots E1 and E2 was illustrated in Fig. 10. As shown in Fig. 10, the residual stress of the ingot after annealing treatment is obviously less than that of the sand cooling treatment. For ESR ingots E1 and E2, the average residual stress in the *H* direction was 622.27 and 431.81 MPa, respectively. The average residual stress in the *X* direction was 493.56 and 56.48 MPa,

respectively. This indicates that the annealing treatment plays a role in reducing residual stress through decreasing the thermal gradient across the ingot.

In order to compare the differences between the two processes, the microstructures of ingots E1 and E2 were observed, as shown in Fig. 11. The secondary dendrite spacing values of ESR ingots E1 and E2 were measured and the mean values are listed in Table 4. As shown in Table 4, the secondary dendrite spacing of the two processes is not significantly different.



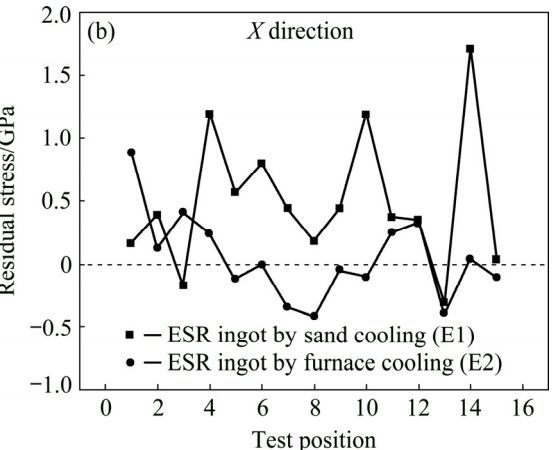


Fig. 10 Comparison of residual stresses in ESR ingots E1 and E2 in H(a) and X(b) directions

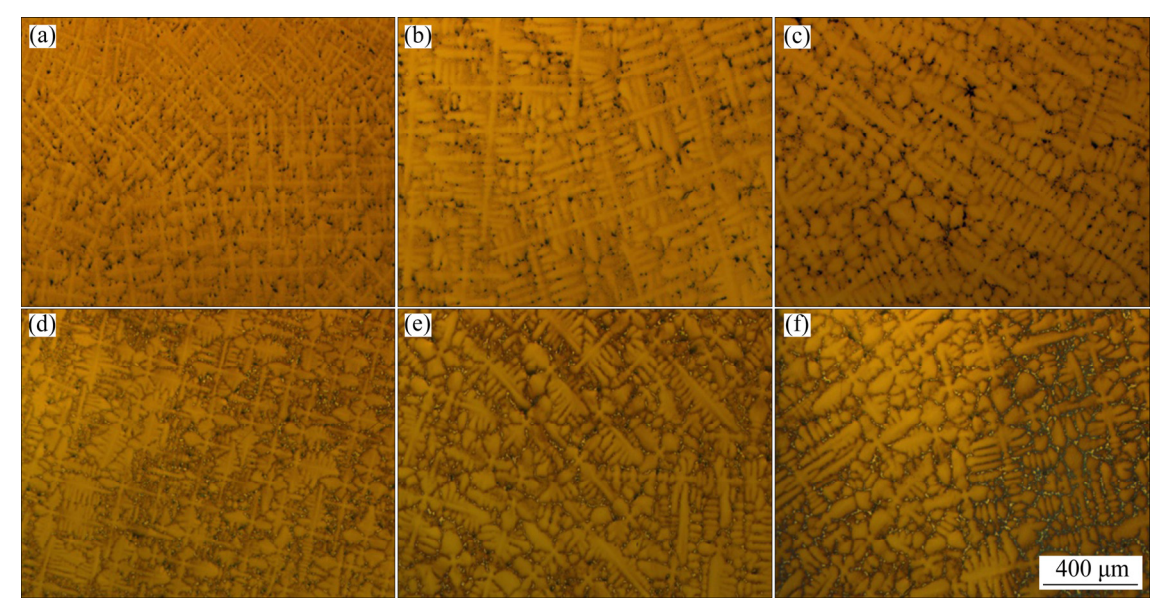


Fig. 11 Microstructures of samples at different positions: (a) Edge of ingot E1; (b) R/2 of ingot E1; (c) Center of ingot E1; (d) Edge of ingot E2; (e) R/2 of ingot E2; (f) Center of ingot E2 (R is radius of sample)

Table 4 Secondary dendrite spacing values of ESR ingots E1 and E2 (µm)

Parameter	Edge of E1	R/2 of E1	Center of E1	Edge of E2	<i>R</i> /2 of E2	Center of E2
Mean	69.21	99.96	112.87	68.25	98.64	110.35
Standard deviation	2.34	8.76	11.75	3.28	9.32	10.63

The segregation coefficients of the two ingots were then measured quantitatively, as listed in Table 5. Figure 12 illustrates the results of segregation for ESR ingots E1 and E2. The segregation inclination of the two processes is not significantly different. The main factor that affects the secondary dendrite spacing and segregation is the cooling rate during solidification. Because the solidification conditions of the two ingots are the same, the dendrite

structure and segregation of the two ingots are not significantly different.

The effect of annealing treatment on the microstructure and cracking formation was discussed below. Firstly, solidification conditions in the two cooling processes are the same, so their solidification microstructures are also the same, such as dendritic structure (Fig. 11) and segregation situation (Fig. 12). In addition, volume fraction of

Table 5 Segregation coefficients for ESR ingots E1 and E2

T ,	E1 .		Edge			<i>R</i> /2		Center			
Ingot	Element	w ₁ /wt.%	w ₂ /wt.%	k	w ₁ /wt.%	w ₂ /wt.%	k	<i>w</i> ₁ /wt.%	w ₂ /wt.%	k	
	Al	3.20	3.11	0.97	3.41	3.14	0.92	3.44	3.10	0.90	
	Ti	2.97	3.52	1.19	3.26	4.16	1.27	2.85	4.39	1.54	
	Ni	54.34	54.18	1.00	55.20	54.74	0.99	56.70	55.24	0.97	
	W	2.76	2.05	0.74	2.72	1.66	0.61	2.79	1.65	0.59	
E1	Nb	2.68	4.37	1.63	2.16	4.51	2.09	2.08	5.61	2.70	
	Cr	13.11	11.88	0.91	12.71	11.20	0.88	12.06	10.13	0.84	
	Mo	4.33	4.53	1.05	4.15	4.54	1.10	3.73	4.65	1.25	
	Co	15.85	15.61	0.98	15.65	15.35	0.98	15.53	14.51	0.93	
	V	0.77	0.75	0.98	0.75	0.71	0.95	0.81	0.73	0.89	
	Al	3.52	3.36	0.95	3.50	3.32	0.95	3.46	3.12	0.90	
	Ti	3.25	3.93	1.21	3.16	4.15	1.31	2.90	4.34	1.50	
	Ni	54.59	53.88	0.99	54.65	53.49	0.98	56.47	54.72	0.97	
	W	2.50	2.33	0.93	2.99	1.82	0.61	2.81	1.65	0.58	
E2	Nb	2.54	4.07	1.60	2.37	4.93	2.08	2.08	5.57	2.69	
	Cr	13.12	12.11	0.92	12.68	11.78	0.93	11.97	10.41	0.87	
	Mo	4.36	4.57	1.05	4.14	4.58	1.11	3.73	4.59	1.23	
	Co	15.31	14.99	0.98	15.71	15.19	0.97	15.79	14.91	0.94	
	V	0.81	0.77	0.95	0.80	0.74	0.92	0.80	0.69	0.87	

 $\overline{w_1}$ and $\overline{w_2}$ represent element contents in dendrite and interdendrite, respectively

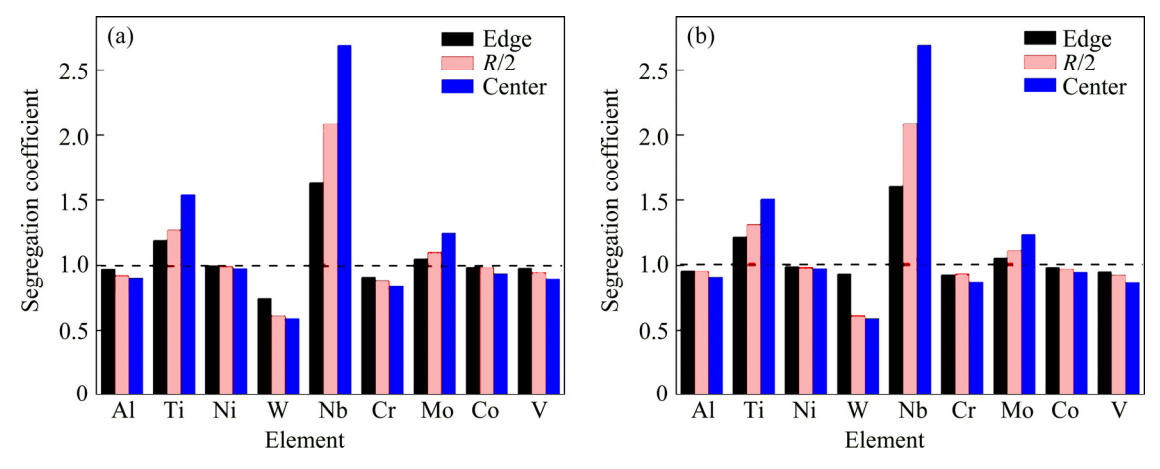


Fig. 12 Segregation coefficients for ESR ingots E1 (a) and E2 (b)

brittle phases cannot change too much, as shown in Fig. 13. Secondly, the current ESR process has been optimized, and thus the solidification microstructure cannot be improved by reducing volume fraction of brittle phases. Therefore, controlling the cooling conditions after solidification is a solution that can be carried out at present. Through slow cooling after solidification, thermal stress can be reduced on one hand, and stress caused by quick precipitation of γ' can be reduced on the other hand. Finally, a non-cracking ingot is obtained. After measurement, the size of γ' particle for ingot E1 is not uniform and the average size is smaller than that of ingot E2, as shown in Fig. 14. Thirdly, the average cooling rates after ESR for sand cooling and furnace cooling are 12.5 and 2.9 °C/h, respectively. There was indeed some difference in the γ' size due to different cooling rates, as shown in Figs. 14 and 15.

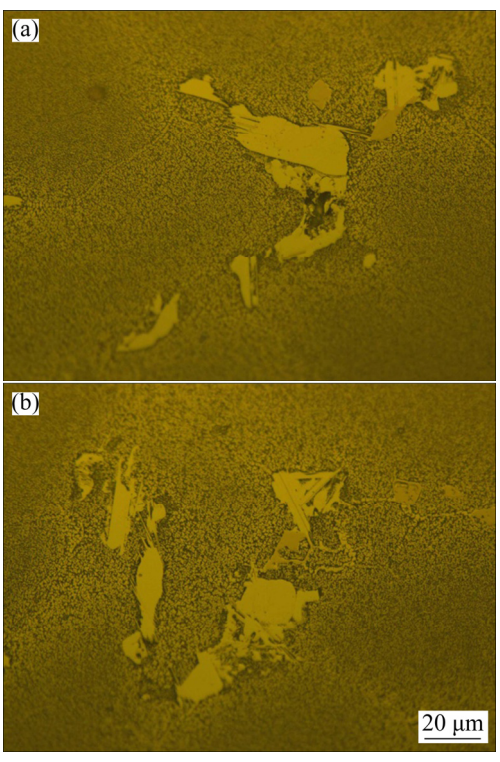


Fig. 13 Morphologies of brittle phase at center positions of ESR ingots E1 (a) and E2 (b)

Figure 14 illustrates the size distribution characteristics of the γ' phase of the two processes. Obviously, the size of γ' particle for ingot E1 is not uniform and the average size is smaller than that of ingot E2. That is to say, the microstructure becomes relatively homogeneous through the annealing treatment. The smaller the size of γ' phase is, the

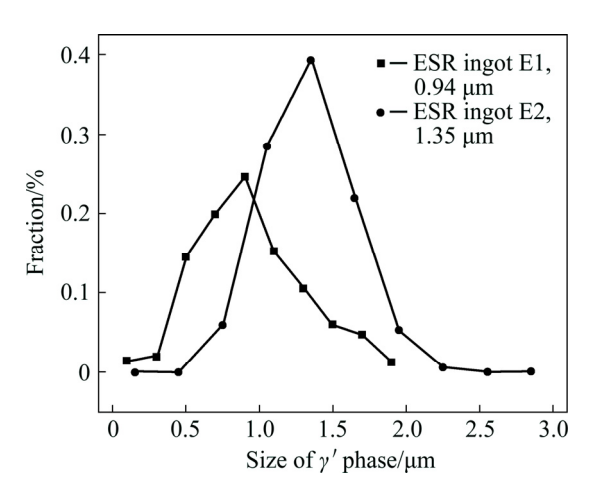


Fig. 14 Statistical size of γ' particle at center positions of ESR ingots E1 and E2

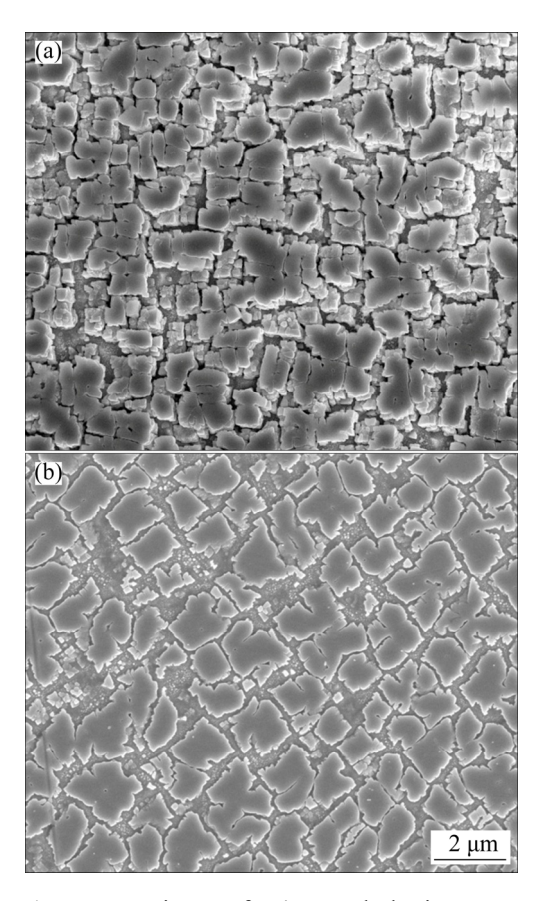


Fig. 15 Comparison of γ' morphologies at center positions of ESR ingots E1 (a) and E2 (b)

more the γ/γ' interfaces exist in the ingot. During the cooling process, the higher residual stress generated by the volume change would be concentrated at the interface. The phase interface is a kind of crystal defect, the capacity of bearing residual stress is bound to be less than that within the phase. Therefore, this size distribution of ingot E2 allows the matrix to accommodate more strain,

which reduces the possibility of cracking by reducing the strain concentration around the precipitate phase. Improving the ductility of the as-cast GH4151 alloy via controlling the size and distribution characteristics is also very helpful for decreasing the cold cracking tendency.

4 Conclusions

- (1) The characteristics of cracking for the as-cast GH4151 ingot were shown clearly in the fracture morphology and microstructure, indicating that the mechanism of crack formation is the cold crack formed during the cooling process.
- (2) Cold cracking is closely related to the ductility, and the ductility in the as-cast GH4151 ingot is affected by severe segregation, complex precipitation phase types and uneven γ' phase distribution.
- (3) By means of XRD, SEM and EPMA, the main phases of the alloy include γ matrix, γ' phase, (Nb,Ti)C phases, η phase, $\gamma+\gamma'$ phase, Laves phase and Ni₅Ce phase. The strain was generated around the precipitate phases and finally cracks appeared due to their different linear shrinkage coefficients.
- (4) The annealing treatment controlling the residual stress and the size and morphology of γ' phase was performed. The annealing treatment played a role in reducing residual stress through decreasing the thermal gradient across the ingot. And after annealing treatment, the size of γ' particle was more uniform and the average size was larger. This size distribution of γ' phase allows the matrix to accommodate more strain, which reduces the possibility of cracking by reducing the strain concentration around the precipitate phases.

References

- [1] ZHANG Peng, ZHU Qiang, CHEN Gang, QIN He-yong, WANG Chuan-jie. Grain size based low cycle fatigue life prediction model for nickel-based superalloy [J]. Transactions of Nonferrous Metals Society of China, 2018, 28: 2102–2106.
- [2] YANG Wan-peng, LI Jia-rong, LIU Shi-zhong, SHI Zhen-xue, ZHAO Jin-qian, WANG Xiao-guang. Orientation dependence of transverse tensile properties of nickel-based third generation single crystal superalloy DD9 from 760 to 1100 °C [J]. Transactions of Nonferrous Metals Society of China, 2019, 29: 558–568.
- [3] JIA Chong-lin, ZHANG Feng-lin, WEI Kang, LV Shao-min. Effective solution treatment can result in improved creep

- performance of superalloys [J]. Journal of Alloys and Compounds, 2019, 770: 166–174.
- [4] HUANG M, ZHU J. An overview of rhenium effect in single-crystal superalloys [J]. Rare Metals, 2016, 35: 127–139.
- [5] SUN Z, TAN X P, DESCOINS M. Revealing hot tearing mechanism for an additively manufactured high-entropy alloy via selective laser melting [J]. Scripta Materialia, 2019, 168: 129–133.
- [6] RIDOLFI M R. Hot tearing modeling: A microstructural approach applied to steel solidification [J]. Metallurgical and Materials Transactions B, 2014, 45: 1425–1438.
- [7] HEYDARIA D, SHAHKARAM FARDA A, BAKHSHIA A. Hot tearing in polycrystalline Ni-based IN738LC superalloy: Influence of Zr content [J]. Journal of Materials Processing Technology, 2014, 214: 681–687.
- [8] FARUP I, DREZET J M, RAPPAZ M. In situ observation of hot tearing formation in succinonitrile–acetone [J]. Acta Materialia, 2001, 49: 1261–1269.
- [9] ESKIN D G, SUYITNO, KATGERMAN L. Mechanical properties in the semi-solid state and hot tearing of aluminium alloys [J]. Progress in Materials Science, 2004, 49: 629–711.
- [10] HU Y L, LIN X, YU X B, XU J J, LEI M, HUANG W D. Effect of Ti addition on cracking and microhardness of Inconel 625 during the laser solid forming processing [J]. Journal of Alloys and Compounds, 2017, 711: 267–277.
- [11] NIE P, OJO O A, LI Z. Numerical modeling of microstructure evolution during laser additive manufacturing of a nickel-based superalloy [J]. Acta Materialia, 2014, 77: 85–95.
- [12] ZHONG M, SUN H, LIU W J, ZHU X F, HE J J. Boundary liquation and interface cracking characterization in laser deposition of Inconel 738 on directionally solidified Ni-based superalloy [J]. Scripta Materialia, 2005, 53: 159–164
- [13] WANG N, MOKADEM S, RAPPAZ M, KURZ W. Solidification cracking of superalloy single- and bi-crystals [J]. Acta Materialia, 2004, 52: 3173–3182.
- [14] CHAUVET E, KONTIS P, JAGLE E A. Hot cracking mechanism affecting a non-weldable Ni-based superalloy produced by selective electron beam melting [J]. Acta Materialia, 2018, 142: 82–94.
- [15] DREZET J M, EVANS A, PIRLING T. Stored elastic energy in aluminium alloy AA 6063 billets: Residual stress measurements and thermomechanical modeling [J]. International Journal of Cast Metals Research, 2012, 25: 110–116.
- [16] LALPOOR M, ESKIN D G, KATGERMAN L. Cold-cracking assessment in AA7050 billets during direct-chill casting by thermomechanical simulation of residual thermal stresses and application of fracture mechanics [J]. Materials Science and Engineering A, 2009, 40: 3304–3313.
- [17] BROWN I H. The role of microsegregation in centreline cold cracking of high strength low alloy steel weldments [J]. Scripta Materialia, 2006, 54: 489–492.
- [18] LALPOOR M, ESKIN D G, BRINK G T, RINK G T, KATGERMAN L. Microstructural features of intergranular

- brittle fracture and cold cracking in high strength aluminum alloys [J]. Materials Science and Engineering A, 2010, 527: 1828–1834.
- [19] ZUO Yu-bo, CUI Jian-zhong, ZHAO Zhi-hao, ZHANG Hai-tao, QIN Ke. Effect of low frequency electromagnetic field on casting crack during DC casting superhigh strength aluminum alloy ingots [J]. Materials Science and Engineering A, 2005, 406: 286–292.
- [20] ZHANG L, ESKIN D G, LALPOOR M, KATGERMAN L. Factors affecting thermal contraction behavior of an AA7050 alloy [J]. Materials Science and Engineering A, 2010, 527: 3264–3270.
- [21] BOENDER W, BURGHARDT A, KLAVEREN E P V, RABENBERG J. Numerical simulation of DC casting: Interpreting the results of a thermo-mechanical model [J]. Light Metals, 2013, 3: 679–684.

一种高 γ '相含量 GH4151 高温合金铸锭的开裂机制

李鑫旭1,2, 贾崇林2, 张 勇2, 吕少敏2, 姜周华1

- 1. 东北大学 冶金学院, 沈阳 110819;
- 2. 中国航发 北京航空材料研究院, 北京 100095

摘 要:研究 GH4151 铸态高温合金裂纹形成基本机理。通过对裂纹特征的分析,确定其开裂机理为冷却过程中形成的冷裂纹。冷裂纹的形成与严重的偏析、复杂的析出相和 y'相分布的不均匀性密切相关。冷却过程中,由于不同析出相线性收缩系数的不同,在析出相周围会产生裂纹。提出一种控制残余应力、y' 相大小和形态的退火工艺。退火处理发挥很大作用,通过降低温度梯度减小残余应力以及控制 y'相的尺寸分布,从而减少析出相周围的应变集中。

关键词: GH4151 合金; 铸锭; 开裂机制; 残余应力; γ'相

(Edited by Wei-ping CHEN)